

A General Coupled Mathematical Model of Electromagnetic Phenomena, Two-Phase Flow, and Heat Transfer in Electroslag Remelting Process Including Conducting in the Mold

QIANG WANG, ZHU HE, BAOKUAN LI, and FUMITAKA TSUKIHASHI

A transient three-dimensional finite-volume mathematical model has been developed to investigate the coupled physical fields in the electroslag remelting (ESR) process. Through equations solved by the electrical potential method, the electric current, electromagnetic force (EMF), and Joule heating fields are demonstrated. The mold is assumed to be conductive rather than insulated. The volume of fluid approach is implemented for the two-phase flow. Moreover, the EMF and Joule heating, which are the source terms of the momentum and energy sources, are recalculated at each iteration as a function of the phase distribution. The solidification is modeled by an enthalpy-porosity formulation, in which the mushy zone is treated as a porous medium with porosity equal to the liquid fraction. An innovative marking method of the metal pool profile is proposed in the experiment. The effect of the applied current on the ESR process is understood by the model. Good agreement is obtained between the experiment and calculation. The electric current flows to the mold lateral wall especially in the slag layer. A large amount of Joule heating around the metal droplet varies as it falls. The hottest region appears under the outer radius of the electrode tip, close to the slag/metal interface instead of the electrode tip. The metal pool becomes deeper with more power. The maximal temperature increases from 1951 K to 2015 K (1678 °C to 1742 °C), and the maximum metal pool depth increases from 34.0 to 59.5 mm with the applied current ranging from 1000 to 2000 A.

DOI: 10.1007/s11663-014-0158-0

© The Minerals, Metals & Materials Society and ASM International 2014

I. INTRODUCTION

ELECTROSLAG remelting (ESR) process has been used widely to produce high-performance alloys dedicated to critical application such as hot work tool steels, nickel base alloys, the manufacture of components in aerospace- and land-based turbines, *etc.*^[1] Figure 1 shows a schematic of the ESR process. The passage of an alternating or direct current from the electrode to the baseplate creates Joule heating in the highly resistive calcium fluoride-based slag that is sufficient to melt the electrode. The interaction between the self-induced magnetic field and the current gives rise to the EMF. Metal droplets sink through the less dense slag to form a liquid metal pool in the water-cooled mold. Solidification occurs continuously at the metal pool-solid interface, and the metal pool profile is determined by a dynamic heat and material balance. The structure and

composition of the remelted ingot are improved by the controlled solidification and chemical refinement, which strongly depend on the magnetohydrodynamic (MHD) flow and heat transfer.^[2]

As shown in Figure 2, the radial electrical resistance of the slag skin layer is smaller than the vertical resistance of the metal. The electric current tends to choose a less resistive way. We have reason to believe that the electric current would flow to the baseplate through the mold lateral wall.

A number of fundamental views involving experimental and numerical studies of the ESR process are presented in the literature. Choudhary *et al.*^[3] measured the velocity field in a room temperature model of an ESR system. Two vortexes were observed, and the maximal velocity increased linearly with the applied current. The thermal behavior, however, was not included in their experiment. Dilawari and Szekely^[4] developed a two-dimensional (2D) axisymmetric mathematical model. The EMF, fluid flow, and heat transfer were studied. The maximum temperature increased from 2000 K to 2060 K (1727 °C to 1787 °C) with the current ranging from 36 kA to 45 kA. The solidification was not studied in their work. Ferng *et al.*^[5] used the numerical simulation to study the uncoupled physical fields in the ESR unit. The solidification was taken into account. The metal pool became deeper with more power. Weber *et al.*^[6] established a coupled 2D axisymmetrical model, which accounts for the MHD flow, temperature fields, and solidification. The metal droplet behavior was not found in their work. Li

QIANG WANG, Ph.D. Candidate, and BAOKUAN LI, Professor, are with the School of Materials and Metallurgy, Northeastern University, Wenhua Road 3-11, Heping District, Shenyang, 110819, People's Republic of China. Contact e-mail: libk@smm.neu.edu.cn
ZHU HE, Associate Professor, is with the Key Laboratory for Ferrous Metallurgy and Resources Utilization, Ministry of Education, Wuhan University of Science and Technology, Wuhan, 430081, People's Republic of China. FUMITAKA TSUKIHASHI, Professor, is with the Department of Advanced Materials Science, Graduate School of Frontier Sciences, The University of Tokyo, 5-1-5 Kashiwanoha, Kashiwa, Chiba, 277-8561, Japan.

Manuscript submitted November 25, 2013.

Article published online August 22, 2014.

et al.^[7] built a 3D finite-element model of the process. The electromagnetic and temperature fields were revealed. The flow, however, was not taken into account. Kharicha *et al.*^[8] simulated the electric field in an ESR mold without the electric insulation hypothesis. They found that the electric current occurring through the mold could modify the hydrodynamic.

It is hard to find a comprehensive description of the ESR process in literature. In order to spread the application of the ESR, a deeper understanding must be developed. In the present work, a transient 3D finite-volume mathematical model has been proposed for studying the coupled electromagnetic phenomena, two-phase flow, and temperature distribution in an ESR unit including the conducting in the mold. Experiments are conducted to validate the model, and the metal pool profiles are marked by an innovative method in experiments. The model is employed to investigate the effect of the applied current on the process.

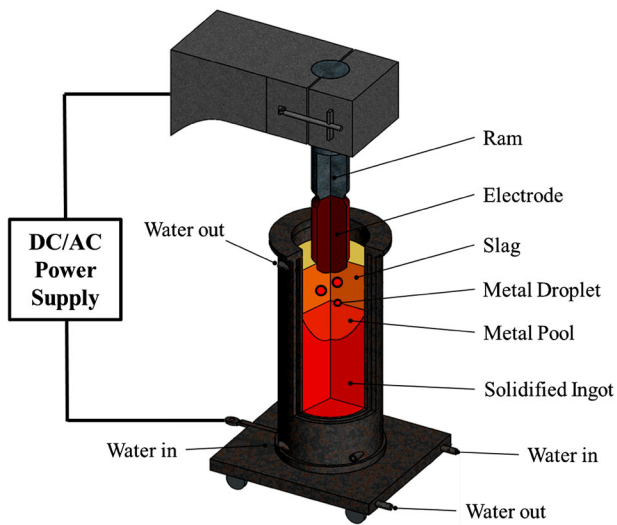


Fig. 1—(Color figure available online) Schematic of electroslag remelting process.

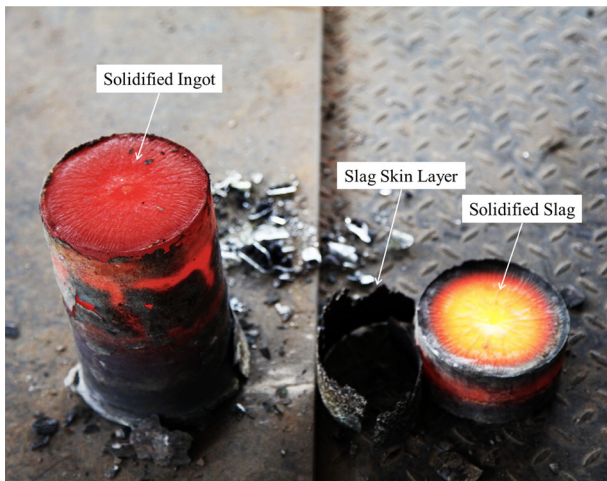


Fig. 2—(Color figure available online) Remelted ingot and solidified slag in the experiment.

II. EXPERIMENTAL PROCEDURE

Experiments have been carried out using a mold with an open-air atmosphere as shown in Figure 3. The mold is made by the copper. The inner diameter, height, and mold wall thickness are 120, 600, and 65 mm, respectively. The applied current used in experiments varies between 1000 and 2000 A with a frequency of 50 Hz. The consumable electrode is the AISI 201 stainless steel with a 55-mm diameter. In order to mark the metal pool profile, the electrode is divided into several pieces, and connected through welding with pieces of high nickel alloy as shown in Figure 3. The metal pool profiles, therefore, are marked due to different colors. This approach is first proposed which can mark the metal pool profiles very well. The slag composition is composed of the calcium fluoride, 75 mass pct, and the aluminum oxide, 25 mass pct. The slag cap thickness is kept at 60 mm. In experiments, the magnetic flux density is measured by the Gauss Meter WT10E, and the temperature is measured every 10 minutes by the disposable W3Re/W25Re thermocouple.^[2,9–11]

III. MATHEMATICAL MODELING

Figure 4(a) displays the mesh model and computation domain. In order to simplify the calculation, some key hypotheses are made as follows:^[12–14]

- The operation is supposed to be steady state. The perturbation and electrode movement are neglected.
- The density of slag and metal is assumed to be dependent on temperature. Besides, the effect of temperature on slag electrical conductivity is also included. Other properties of slag and metal are assumed to be constant.^[15]
- The shape and immersion depth of the electrode remain unchanged. In order to close the actual, the electrode shape used in the model is determined by the experimental photo as shown in Figure 4(b).

A. Electromagnetic Phenomena

An alternating current is used in the ESR process. The electromagnetic field is described by Maxwell's equations:^[8,9]

$$\nabla \times \vec{H} = \vec{J} + \frac{\partial \vec{D}}{\partial t} \quad [1]$$

$$\nabla \times \vec{E} = -\frac{\partial \vec{B}}{\partial t} \quad [2]$$

$$\nabla \cdot \vec{B} = 0. \quad [3]$$

Current displacement is much lower than the electric conduction, which is valid if the electrical conductivity is not too small.

The constitutive equations for the electromagnetic field are expressed as follows:

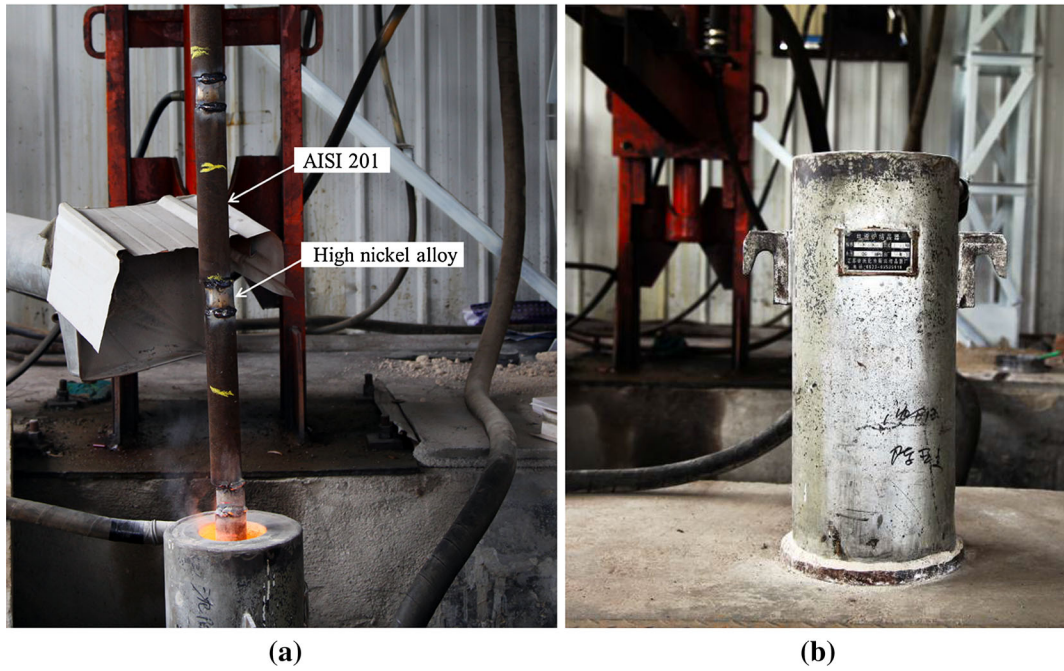


Fig. 3—(Color figure available online) (a) Special electrode assembled by the AISI 201 and high nickel alloy and (b) mold used in the experiment.

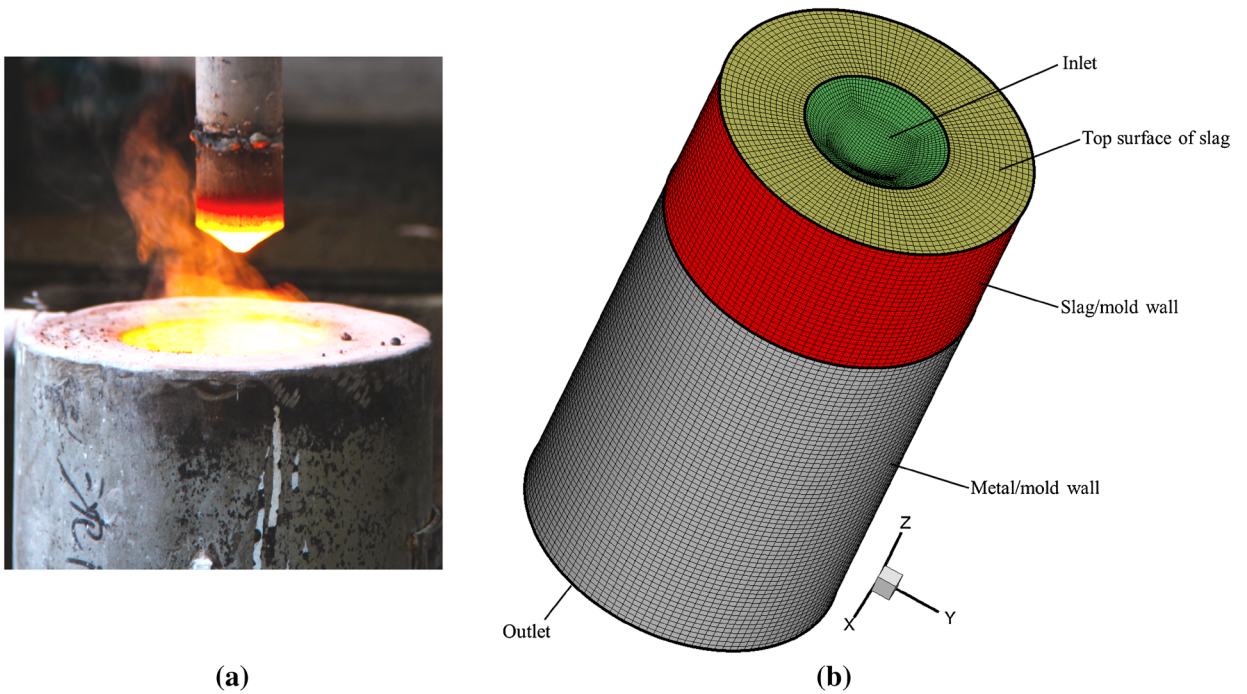


Fig. 4—(Color figure available online) (a) Electrode tip shape in the experiment (b) Mesh model of the computation domain.

$$\vec{B} = \mu \vec{H} \quad [4]$$

$$\vec{J} = \sigma (\vec{E} + \vec{u} \times \vec{B}). \quad [5]$$

According to the study made by Dilawari and Szekely,^[16] the magnetic Reynolds number, which expresses the measure of the ratio of the magnetic convection to magnetic diffusion, remains very low in the ESR process. Thus, Eq. [5] can be simplified as

$$\vec{J} = \sigma \vec{E}. \quad [6]$$

The electrical potential approach is employed to solve the governing equations mentioned above.^[17] It consists in simultaneously solving the electrical potential ϕ as well as the magnetic potential vector \vec{A} equations. The electrical potential equation is extracted from the conservation of the electric current:

$$\nabla \cdot \vec{J} = 0 \text{ with } \vec{J} = -\sigma \frac{\partial \vec{A}}{\partial t} - \sigma \nabla \phi. \quad [7]$$

On the other hand, the magnetic potential vector is related to the magnetic field by

$$\vec{B} = \nabla \times \vec{A}. \quad [8]$$

The electromagnetic field can be decomposed into a time-dependent and a steady component when the electromagnetic field is harmonic. Numerical studies on electromagnetically driven flows show that the alternating current period which controls the variation period of the electromagnetic field is much shorter than the momentum response time of the liquid metal if its frequency is larger than 5 Hz.^[18] Therefore, the time-averaged EMF and Joule heating can be expressed as

$$\vec{F}_e = \vec{J} \times \vec{B} \quad \text{and} \quad Q_{\text{Joule}} = \frac{\vec{J} \cdot \vec{J}}{\sigma}. \quad [9]$$

B. Fluid Flow

The flow is modeled with the continuity equation and time-averaged Navier–Stokes equations:

$$\frac{\partial \rho}{\partial t} + \nabla \cdot (\rho \vec{u}) = 0 \quad [10]$$

$$\left[\frac{\partial (\rho \vec{u})}{\partial t} + \nabla \cdot (\rho \vec{u} \otimes \vec{u}) \right] = -\nabla p + \mu_{\text{eff}} \nabla^2 \vec{u} + \vec{F}_e + \vec{F}_b + \vec{F}_p, \quad [11]$$

where \vec{F}_e is the EMF and \vec{F}_b , the buoyancy force, is determined by the Boussinesq approximation:

$$\vec{F}_b = \rho \beta \vec{g} (T - T_{\text{ref}}). \quad [12]$$

The source term \vec{F}_p is employed to gradually block the velocity to zero in the mushy zone as will be described below in the next section.^[12]

The movement of the slag and metal in the ESR process is weakly turbulent, as previously shown by Jardy *et al.*^[14] The RNG k – ε turbulence model is used to calculate the turbulent viscosity. The standard k – ε turbulence model was developed for flows with a high Reynolds number, but the RNG k – ε turbulence model is able to also capture the behavior of flows with lower

Reynolds number with an appropriate treatment of the near-wall region:

$$\frac{\partial}{\partial t}(\rho k) + \frac{\partial}{\partial x_i}(\rho k u_i) = \frac{\partial}{\partial x_j} \alpha_k \mu_{\text{eff}} \frac{\partial k}{\partial x_j} + G_k + G_b - \rho \varepsilon - Y_M + S_k \quad [13]$$

$$\frac{\partial}{\partial t}(\rho \varepsilon) + \frac{\partial}{\partial x_i}(\rho \varepsilon u_i) = \frac{\partial}{\partial x_j} \left(\alpha_\varepsilon \mu_{\text{eff}} \frac{\partial \varepsilon}{\partial x_j} \right) + C_{1\varepsilon} \frac{\varepsilon}{k} (G_k + C_{3\varepsilon} G_b) - C_{2\varepsilon} \rho \frac{\varepsilon^2}{k} - R_\varepsilon + S_\varepsilon. \quad [14]$$

An enhanced wall function is employed with the RNG k – ε turbulence model, in particular, since liquid metal has a low Prandtl number.

The interface between the metal and slag is tracked with the geometric reconstruction VOF approach, since it is a robust, powerful, and extensively applied technique. An important parameter—the volume fraction of fluid α —is solved simultaneously everywhere in the domain. It requires the addition of the following conservation equation:

$$\frac{\partial \alpha}{\partial t} + \nabla \cdot (\alpha \vec{u}) = 0. \quad [15]$$

α is defined as the local fraction of the space occupied by the component that is tracked. Basically, when the control volume is empty (no traced fluid), the value of α is 0. When the cell is full with the fluid considered, the value of α is 1, and when the interface between the fluid tracked and another fluid cuts through the cell, α is a number between 0 and 1. During the calculation, the fluid volume fraction in the domain is consistent with the resolution of the other flow quantities. Furthermore, knowing the α field in the domain allows locating the slag/metal interface. A single set of governing equations is shared by the metal and slag. The local physical properties in the governing equations are determined by the local value of α .^[19–21]

In addition, the surface tension can play an important role on the motion of metal droplet as well as on the oscillation of the slag/metal interface.^[22] The continuum surface force model is implemented to consider the surface tension in present work. It consists in introducing a source term in the momentum equations when α is neither 0 nor 1, *i.e.*, at the slag/metal interface.^[23]

C. Heat Transfer and Solidification

To obtain a precise prediction of the temperature distribution and solidification in the ESR process, the energy conservation equation of the enthalpy formulation is employed:

$$\frac{\partial}{\partial t}(\rho H) + \nabla \cdot (\rho \vec{u} H) = \nabla \cdot (k_{\text{eff}} \nabla T) + Q_{\text{Joule}}. \quad [16]$$

Table I. Physical Property, Geometry, and Operating Conditions of the ESR System

Parameter	Value
<i>Physical properties of metal</i>	
Density (kg/m ³)	7500
Liquidus/solidus (K)	1723/1588
Dynamic viscosity (Pa s)	0.0061
Latent heat of fusion (kJ/kg)	270
Thermal conductivity (W/m K)	30.52
Specific heat (J/kg K)	752
Electric conductivity (Ω ⁻¹ m ⁻¹)	7.14 × 10 ⁵
Magnetic permeability (H/m)	1.257 × 10 ⁻⁶
Thermal coefficient of cubical expansion (K ⁻¹)	1 × 10 ⁻³
<i>Physical properties of slag</i>	
Density (kg/m ³)	2800
Liquidus (K)	1650
Dynamic viscosity (Pa s)	0.0025
Thermal conductivity (W/m K)	10.46
Specific heat (J/kg K)	1255
Electric conductivity (Ω ⁻¹ m ⁻¹)	ln σ = -6769.0/ -6769.0T.T + 8.818
Magnetic permeability (H/m)	1.257 × 10 ⁻⁶
Thermal coefficient of cubical expansion (K ⁻¹)	1 × 10 ⁻⁴
<i>Geometry</i>	
Electrode diameter (m)	0.055
Ingot diameter (m)	0.12
Slag height (m)	0.06
Immersion depth of electrode (m)	0.012
<i>Operating conditions</i>	
Current (A)	1000/1300/1800/2000
Melting rate (kg/s)	0.0078/0.0093/0.0132/0.0147
Frequency (Hz)	50
Temperature of cooling water in and out (K)	288/310
Temperature of air (K)	308
Heat transfer at the slag/mold wall (W/m ² K)	355
Heat transfer at the metal/mold wall (W/m ² K)	310
Heat transfer at the slag/air wall (W/m ² K)	188
Emissivity of top surface of slag	0.6
Interfacial tension between slag and metal (N/m)	0.9

The Joule heating, Q_{Joule} , appears as a source term. The enthalpy of metal and slag is computed as the sum of the sensible enthalpy and the latent heat which is released in the mushy zone:

$$H = h + f_{\ell}L \text{ and } h = h_{\text{ref}} + \int_{T_{\text{ref}}}^T c_p dT. \quad [17]$$

A linear relation between temperature and liquid fraction f_{ℓ} is assumed as follows:^[24-27]

$$f_{\ell} = \frac{T - T_s}{T_l - T_s}. \quad [18]$$

As mentioned above in Eq. [11], the velocity field must be blocked in the solid phase with the term \vec{F}_p . An enthalpy-porosity formulation was used. It treats the mushy zone in the momentum equation as a “pseudo” porous medium in which the porosity gradually decreases from 1 to 0 as the metal solidifies:

$$\vec{F}_p = \frac{(1 - f_{\ell})}{f_1^s} A_{\text{mush}}(\vec{u} - \vec{u}_{\text{cast}}). \quad [19]$$

In the process, the slag level is moved upward slowly as the metal pool is filled by the falling metal droplets. The casting velocity is very small (of the order of 10⁻³ m/s), and therefore it was ignored in Eq. [19].^[24]

Source terms are also added to the equations of RNG k - ϵ turbulence model in the mushy and solidified zones:

$$S_k = \frac{(1 - f_{\ell})^2}{f_1^s} A_{\text{mush}}k \text{ and } S_{\epsilon} = \frac{(1 - f_{\ell})^2}{f_1^s} A_{\text{mush}}\epsilon. \quad [20]$$

D. Metal Droplets

The metal droplet behavior is very critical to the mass, momentum, and heat transfer in the process. Electric current tends to follow the path of least resistance. Therefore, the electric current density is controlled by

the slag-to-metal ratio of electrical conductivity if the electrochemistry is ignored. The effective EMF per unit of volume that applies to the metal droplet, \vec{F}_{ed} , is given by

$$\vec{F}_{ed} = \frac{3}{2} \eta \frac{\sigma_m - \sigma_s}{2\sigma_s + \sigma_m} \vec{j} \times \vec{B}. \quad [21]$$

The validity of the above equation is limited to spherical droplets which is why a correction coefficient, η , is introduced when nonspherical droplets are encountered. Since the EMF is oriented radially (toward the center), it generates a pinch effect and forces metal droplets to move inward and coalesce in the ESR process.^[4,29]

The heat would be transferred from the slag to the metal pool by metal droplets. As a result, the temperature of metal droplets increases significantly during the falling process.

E. Boundary Conditions

1. Electromagnetism

A zero potential is imposed at the inlet. A potential gradient is applied at the outlet. A radial distribution of the current density is considered to account for the skin effect.^[30–32]

$$\frac{\partial \phi}{\partial z} = -\frac{I_{rms} \exp\left(\frac{R-R_{max}}{\delta}\right)}{\sigma_m \pi R_{max}^2}, \delta = \sqrt{\frac{\rho_{em}}{\mu_{0m} \pi f_H}}. \quad [22]$$

The mold lateral walls are described as follows:

$$\text{Model excluding conducting in the mold : } \frac{\partial \phi}{\partial n} = 0 \quad [23]$$

$$\text{Model excluding conducting in the mold : } \frac{\partial \phi}{\partial n} = V_{drop}, \quad [24]$$

where the voltage drop is measured in the experiment.

The magnetic flux density is supposed to be continuous at the inlet and outlet, and negligibly small at the mold lateral wall.^[16]

$$\text{Inlet and outlet : } A_x = A_y = \frac{\partial A_z}{\partial z} = 0 \quad [25]$$

$$\text{Wall : } A_x = A_y = A_z = 0. \quad [26]$$

2. Fluid flow

The melt rates with different applied currents are obtained from experiments and imposed at the inlet. The outflow is applied on the outlet. Besides, a no-slip condition is applied on the wall where the slag and metal are in contact with the mold. At the top surface of slag, a zero shear stress is employed to model this free surface. As the foregoing, the enhanced wall function is used due to the low Prandtl number.^[9]

3. Heat transfer

The temperature of the metal at inlet is given by a parabolic profile, with an approximate 30 K superheat and a peripheral boundary temperature close to the metal liquidus, in order to take the melting process into account in a simplified way.

The top surface of slag is supposed to exchange heat with the surrounding air by natural convection as well as thermal radiation.

The heat loss to the mold lateral wall is expressed by a Robin condition. The heat transfer coefficient depends on many factors. For instance, an air gap appears at the metal/mold wall which diminishes the heat loss due to the shrinkage. Natural convection and thermal radiation are presented in the air gap simultaneously. Because estimating the heat transfer coefficient can be quite

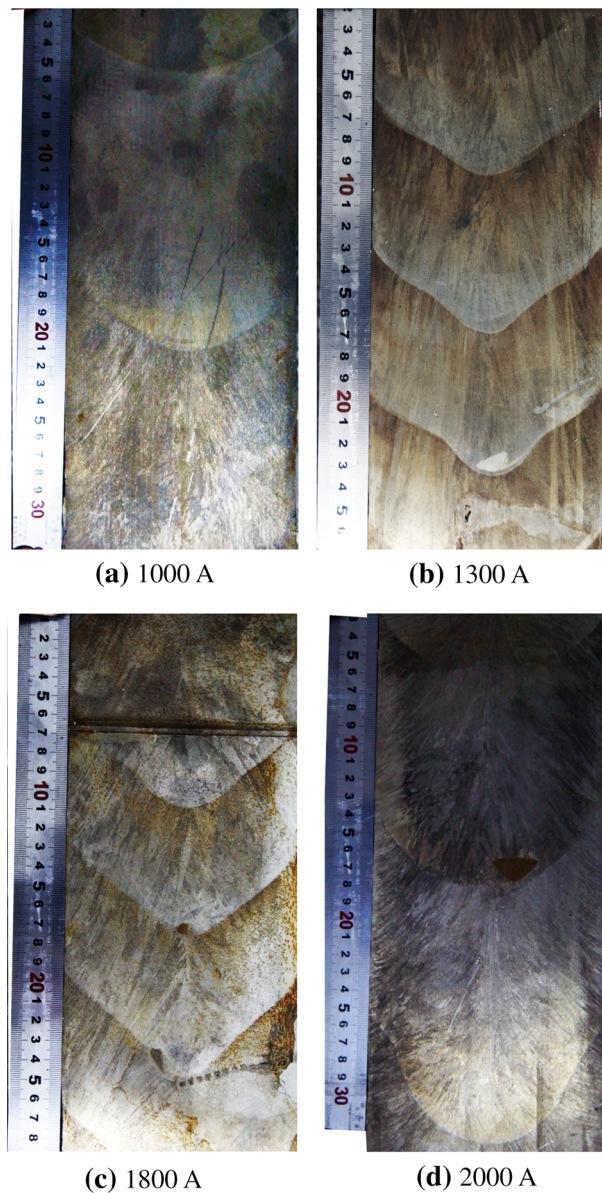


Fig. 5—(Color figure available online) Metal pool profiles and macrostructure at the longitudinal section of the remelted ingot.

complicated, an equivalent heat transfer coefficient of the slag/mold wall and metal/mold wall is deduced from experiments and literatures. The detailed physical properties, geometry, and operating conditions are listed in Table I.^[24,25,33,34]

IV. SOLUTION METHOD

The governing equations have been discretized based on the finite-volume method. The commercial software FLUENT is employed to solve equations. The electromagnetic phenomena are described by the MHD module of FLUENT as well as user-defined functions. Governing equations for the electromagnetic phenomena, two-phase flow, heat transfer, and phase change are solved simultaneously, with an iterative procedure. The EMF and Joule heating are updated at each iteration as a function of the phase distribution and incorporated into the momentum and energy equation as a source terms, as described previously. Before advancing to the next time step, the iterative procedure was continued until all normalized unscaled residuals are less than 10^{-6} . A mesh independence study was performed. Three meshes were considered, respectively, with 260,000, 580,000, and 830,000 control volumes. The deviation

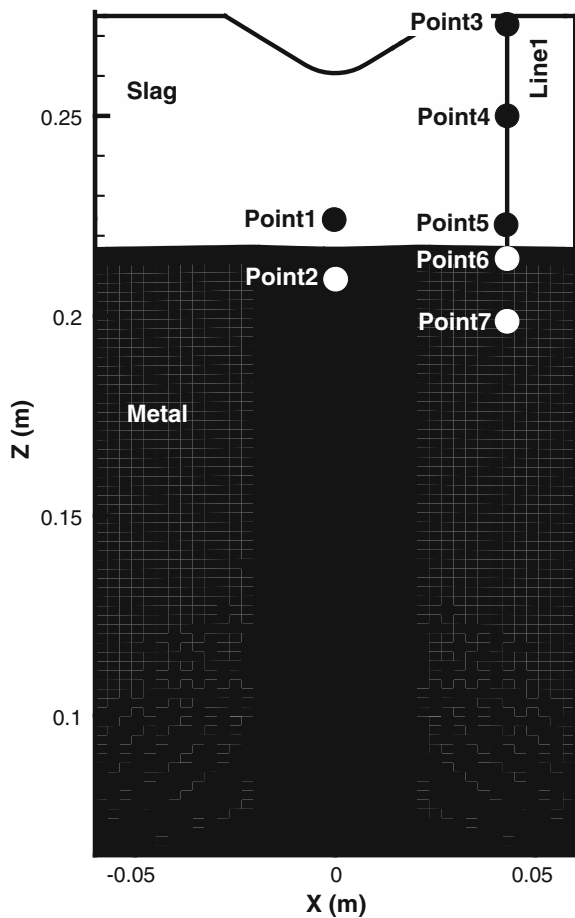


Fig. 6—Schematic of the monitor point and the line.

of the numerical results between the first and second mesh is about 12 pct, while the deviation between the second and the third mesh is approximately 5 pct. Therefore, considering the large computational times involved, the second mesh was retained for the rest of this paper

V. RESULTS AND DISCUSSION

A. Validation of the Mathematical Model

Figure 5 shows the macrostructure of the remelted ingots with four applied currents. The remelted ingots are sectioned longitudinally and then etched with aqua regia. The solidification structure at the bottom grows downward and laterally at the upside, because the direction of the solidification structure is determined by the heat flux. In the initial stage of the process, the heat is dissipated mainly through the baseplate. However, the longitudinal thermal resistance becomes bigger with the growing of the remelted ingot, and the heat is extracted mostly by the lateral wall (Figure 6).

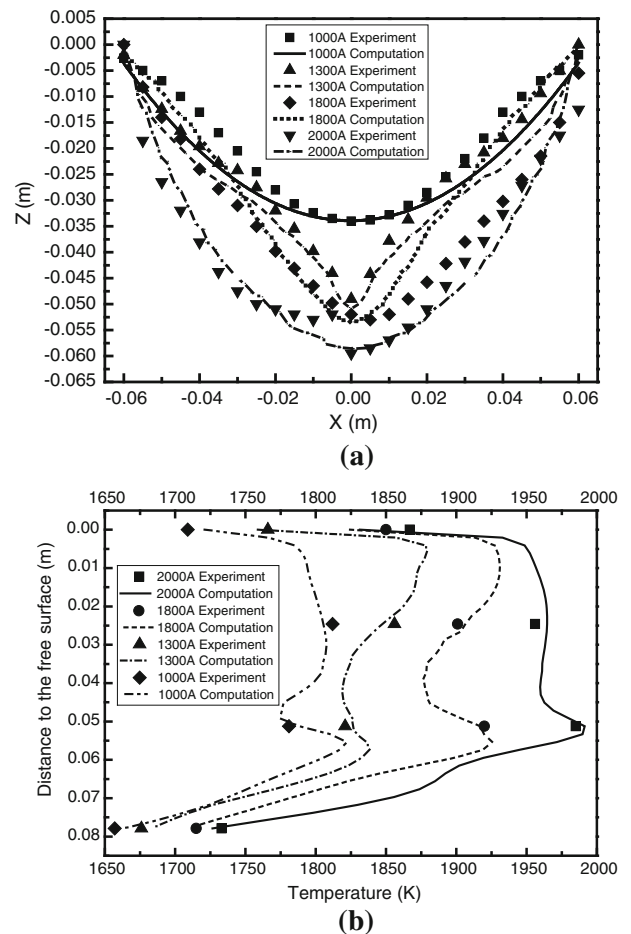


Fig. 7—(a) Comparison of the experimental and calculated metal pool profiles with different applied currents and (b) comparison of the experimental and calculated temperature, the experimental temperature is obtained from point 3, point 4, point 5, and point 7, and the calculated temperature is obtained from line 1.

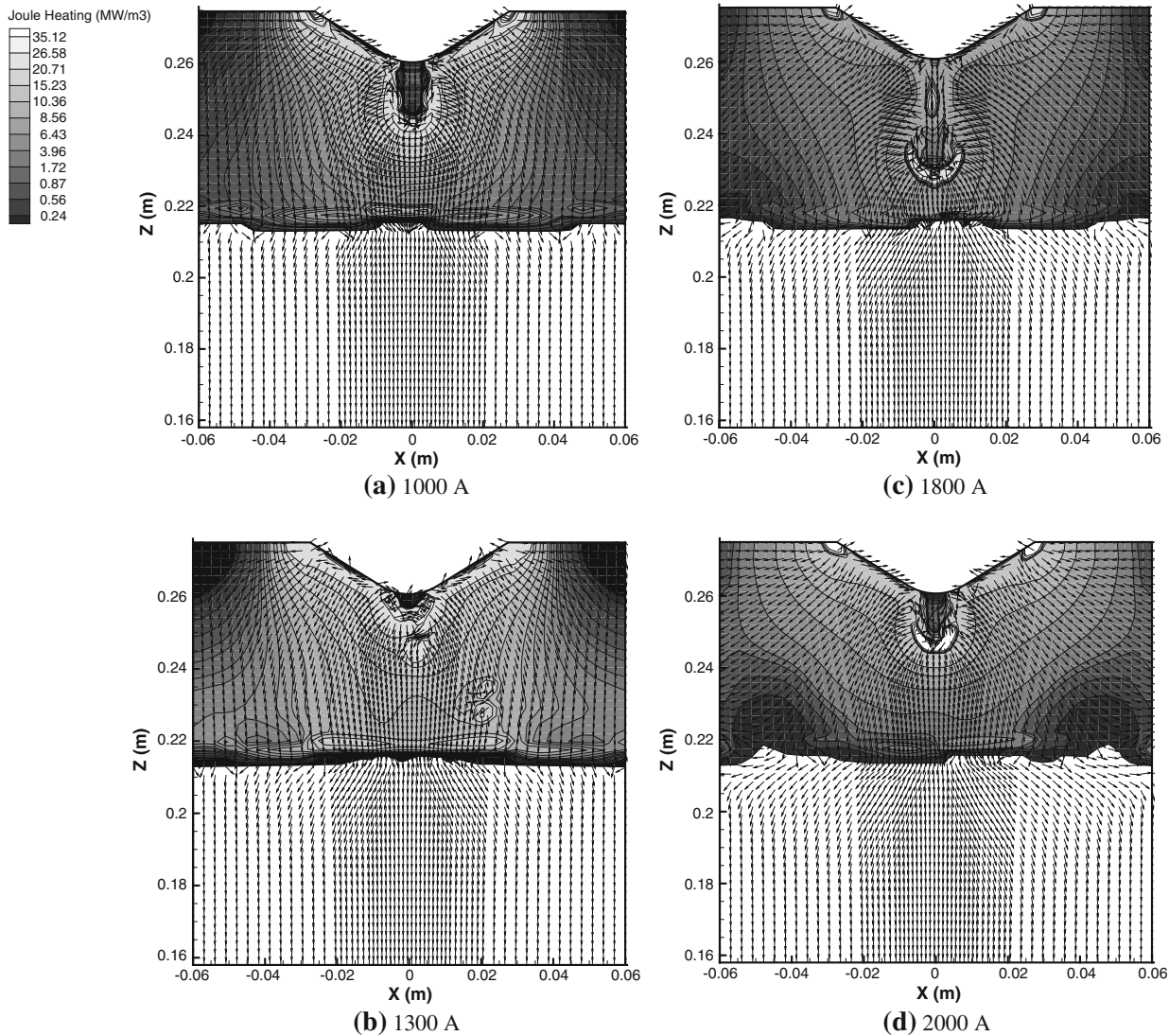


Fig. 8—Electric current field and Joule heating distribution with different applied currents at 5000 s.

Due to the high nickel alloy, the metal pool profiles are marked clearly. The metal pool depth is approximately 33, 42, 45, and 60 mm for an applied current of 1000, 1300, 1800, and 2000 A, respectively. A shallow U-shaped metal pool is observed with an 1000 A applied current. The metal pool becomes deeper with the increasing applied current. The shallow U-shaped profile turns to the deep V-shaped profile gradually. When the applied current is 2000 A, the deep U-shaped metal pool is found. Figures 7(a) and (b) display the comparison of the temperature and metal pool profiles between the experimental measurements and numerical results. The deviation between the measured and calculated results is less than 5 pct. A reasonable agreement is obtained, which indicates the reliability of the model.

B. Electromagnetic and Joule Heating Fields

Figure 8 displays the current density field (isometric vector) and the Joule heating density distribution with

four applied currents at 5000 seconds. Figure 9 presents the EMF field and the phase distribution at 5000 seconds. The electric current tends to go first through the metal which owns a higher electrical conductivity. The current density vector near the lateral wall is oblique rather than vertical, because a part of the electric current passes through the mold, especially in the slag layer, and this portion increases when more current is applied. The current density vector becomes more oblique with the applied current of 2000 A than that with an 1000 A applied current. The comparison of the current density at the lateral wall is presented in Figure 12. Additionally, the skin effect cannot be observed, because the skin effect depth is approximately 85 mm larger than the mold radius. Due to the electrical conductivity difference, the path of the electric current is distorted at the slag/metal interface, which gives rise to a discontinuous EMF. This force, however, is too small to affect the interface movement significantly. It can be inferred that the entrapped slag phenomenon cannot be observed in the ESR furnace.

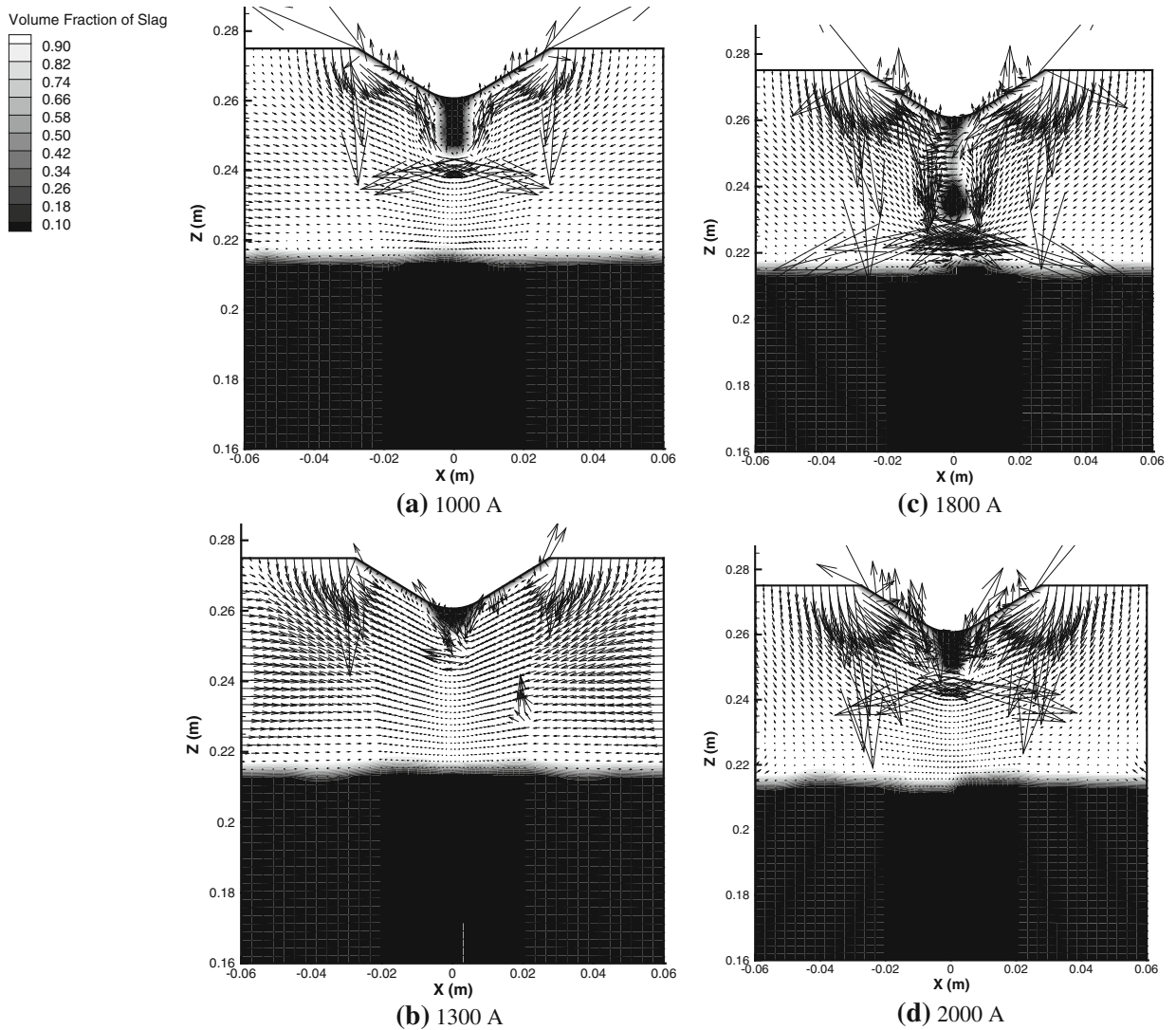


Fig. 9—Electromagnetic force field and phase distribution with different applied currents at 5000 s, the maximum electromagnetic force is 365 N/m^3 .

The Joule heating is mainly generated by the slag. Besides, the Joule heating density is proportional to the current density while inversely proportional to the electrical conductivity. The distribution of the Joule heating density, therefore, is similar to that of the current density. As observed in Figures 8(c) and (d), lots of Joule heating occurs around the metal droplet due to the big current density, and the distribution of Joule effect always varies with the falling metal droplet. The maximal Joule heating density increases with a larger applied current as illustrated in Figure 12. In addition, the minimal Joule heating density is located in the outer side of the top and bottom of the slag layer. When there is more power, the Joule heating density at the outer side of the top of the slag increases, while that at the bottom of the slag decreases. The phenomenon is not observed in previous works in which the mold is assumed to be insulated.^[9,35] The electric currents in the mold and the metal droplet make a strong effect on the ESR process, which should be included in the model. Moreover, an appropriate applied current should be chosen for the process in practice.

The inward EMF generates a pinch effect on the slag as observed in previous works.^[8,36,37] Due to the falling of the metal droplet, the electric current as well as EMF changes significantly. It can be seen that the EMF around the metal droplet tends to block its motion. In previous works, the maximum EMF is found at the top of the slag near the outer radius of the electrode, because the metal droplet is not considered. Here, large EMF also appears around the droplet which affects the residence time of the droplet in the slag.

C. Temperature Distribution

Figure 10 demonstrates the temperature distribution with four applied currents at 5000 seconds. It should be noted that the temperature field due to the combined effect of the Joule heating and flow is different from the one coming from the Joule heating alone. A large amount of the Joule heating is carried out to the metal pool due to the falling of the metal droplet which heats the nearby slag. The hotter region is located in the

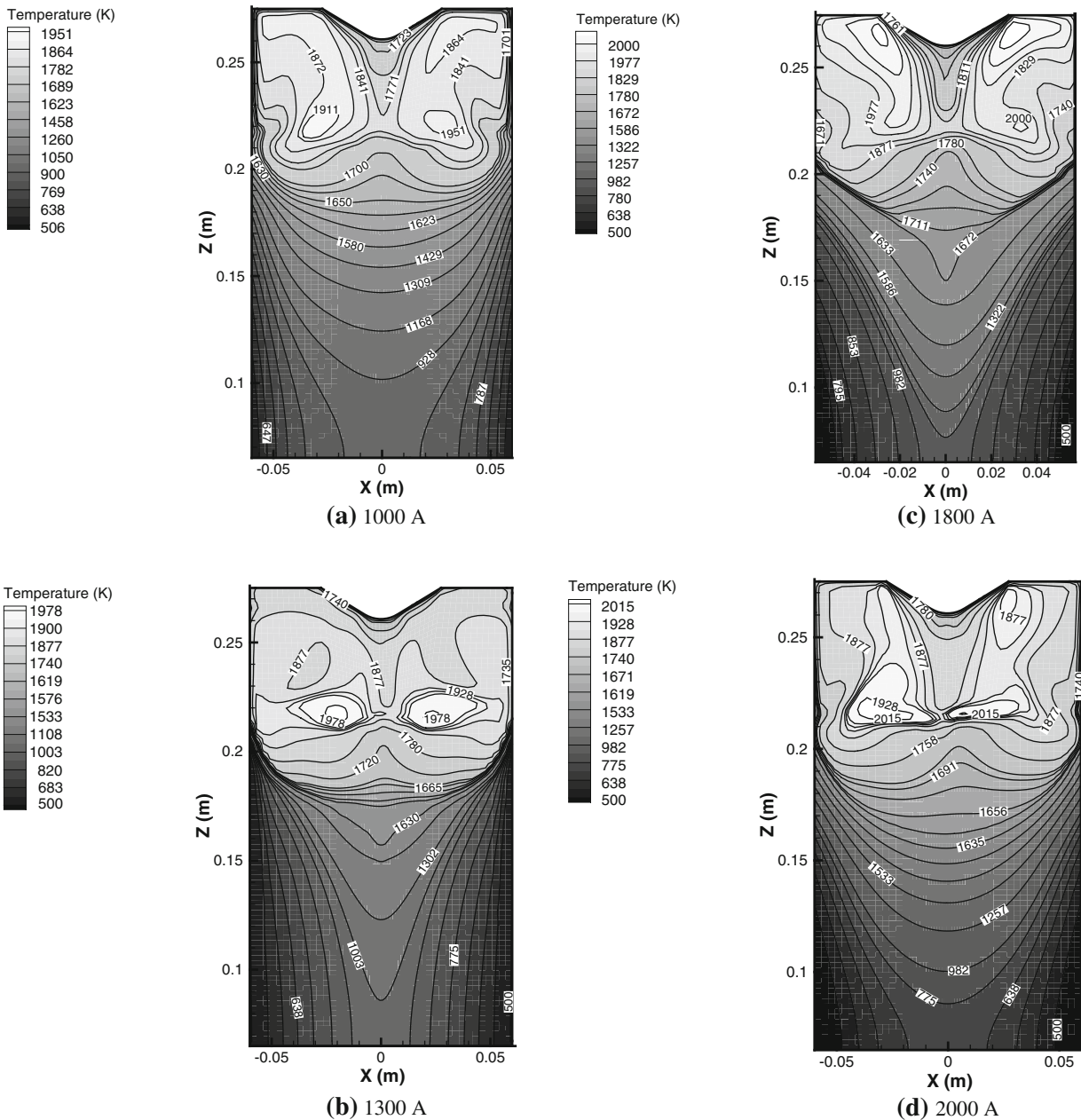


Fig. 10—Temperature distribution with different applied currents at 5000 s.

midradius of the slag if we observe the right side of the figure. Due to the flow, the upper part of the slag at the outer side also owns a higher temperature, while a lower heat generation is observed at the same location. An instability of Rayleigh–Bénard type arises because of the characteristics of the temperature distribution in the slag, *i.e.*, the slag closer to the electrode is colder than the slag underneath this zone.^[7] Besides, the colder slag near the lateral wall owns a big temperature gradient due to the strong cooling. With the increasing applied current, the slag layer becomes hotter, and the maximal temperature increases from 1951 K to 2015 K (1678 °C to 1742 °C) as shown in Figure 13.

On the other hand, the shapes of the isotherms in the metal are also affected by the applied current. The

isotherms shapes in the metal are all parabolic in four cases. However, the curvatures of the parabolic isotherms become larger when the applied current increases. The heat in the metal pool dissipates rapidly with the applied current of 1000 A. A shallow U-shaped isotherm is obtained. The isotherms gradually become steep V shapes, because the current increases and the cooling remains unchanged.

D. Velocity Field and Solidification

Figure 11 shows the velocity field and the solidification with four applied currents at 5000 seconds. Two pairs of vortex are noticed in the slag. As observed the right side of the figure, the heat extracted by the cooling

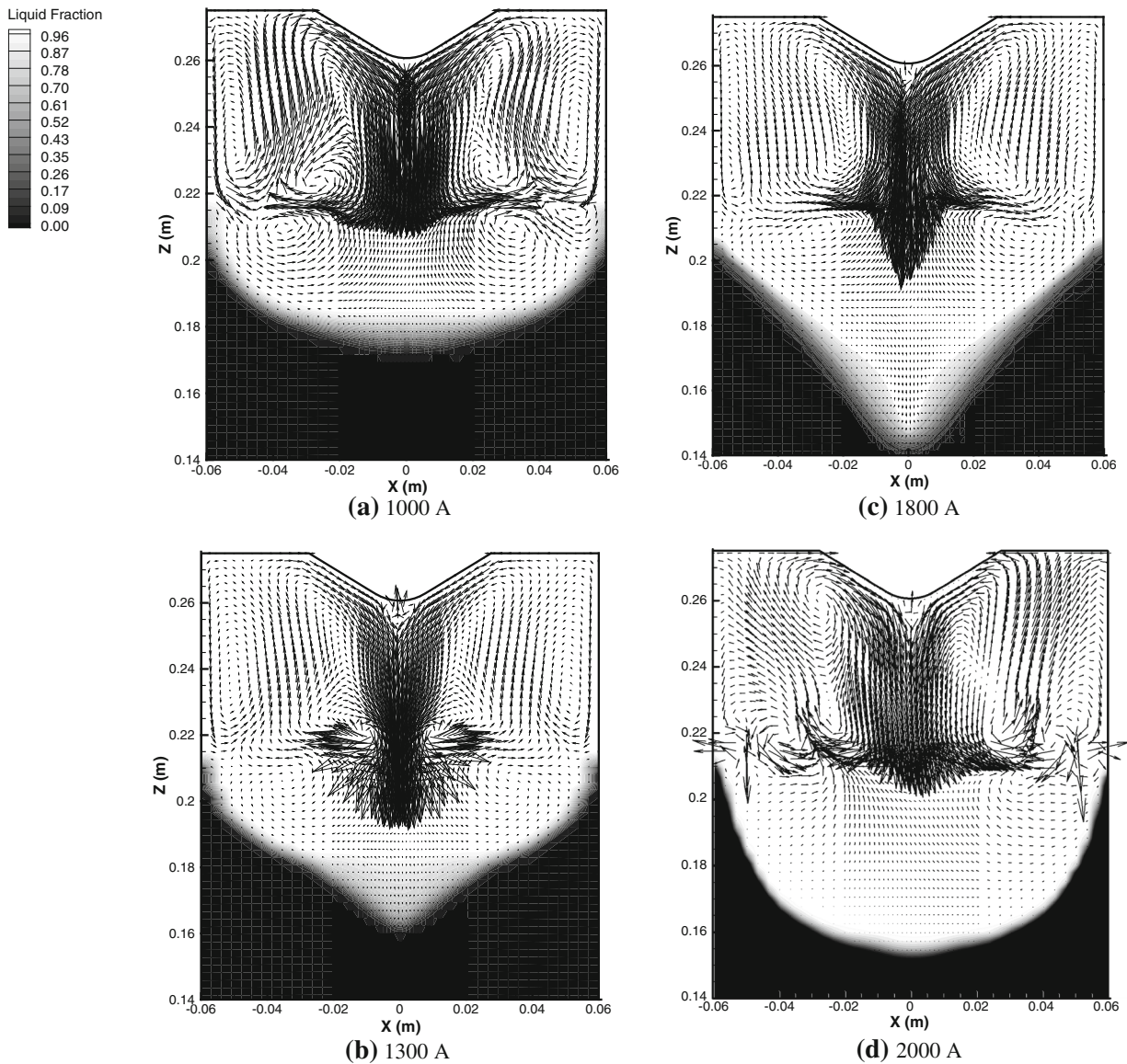


Fig. 11—Velocity field and solidification with different applied currents at 5000 s, the maximum velocity is 0.07 m/s.

water results in a descending movement of the slag at the lateral wall due to buoyancy, driving a stable clockwise circulation. At the center of the slag, a counterclockwise circulation is caused by the EMF and falling metal droplets. It can be deduced that the flow in the center of the slag is controlled by the EMF and falling metal droplets, and the buoyancy dominates the flow closer to the lateral wall. It is a typical flow pattern in small laboratory scale ESR units. With more current is applied, the flow in the middle of the slag becomes stronger, while slower near the lateral wall. Figure 12 reveals the evolution of the maximum turbulent kinetic energy with the applied currents.

The flow in the metal pool is different from that in the slag. It is controlled mainly by the interfacial and buoyancy forces rather than the EMF, because the EMF is small in the metal pool. Two weak vortices are shown in the metal pool. The flow in the vicinity of solidification front is hindered. The maximal velocity in the slag

is around 0.07 m/s, and the velocity in metal pool is much smaller (Figure 13).

The slag/metal interface behavior is crucial to the heat and momentum transfer between the slag and metal pool. The interface oscillates due to falling metal droplets as shown in Figure 14(a). The heat and momentum are carried out to the metal pool by metal droplets. Figure 14(b) indicates the variation of the turbulent kinetic energy with time at point 1. The turbulent kinetic energy increases rapidly when the metal droplet goes through the point. Due to bigger metal droplets, the turbulent kinetic energy at point 1 increases with more power.

Figure 15(a) represents the deformation of the slag/metal interface at different applied currents, and Figure 15(b) shows the evolution of the turbulent kinetic energy with time at point 6. The interface owns a bigger deformation with a larger applied current. The amplitude of the oscillation of the turbulent kinetic energy

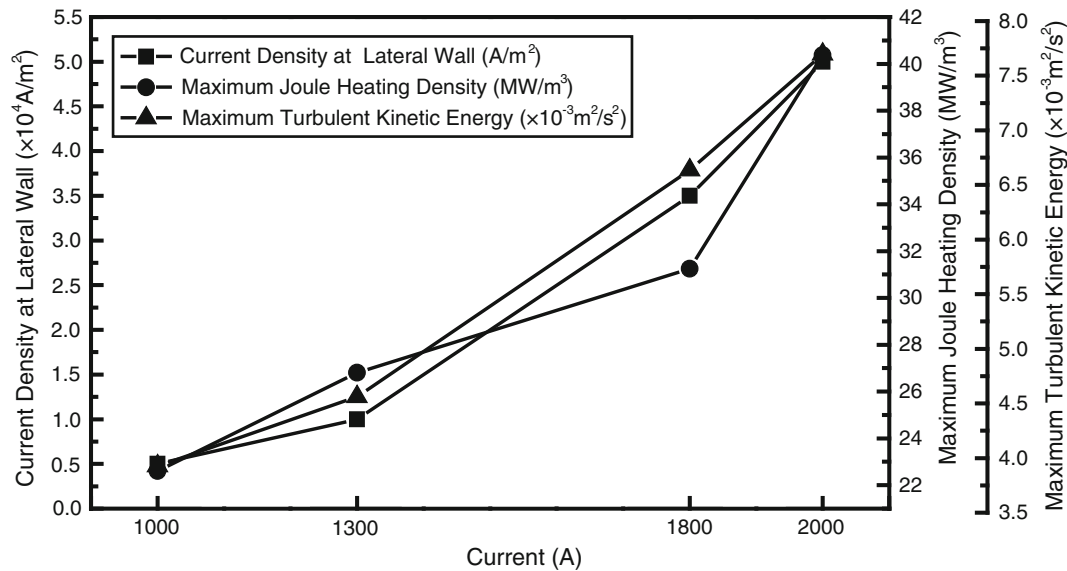


Fig. 12—Comparison of the current density at the lateral wall, the maximum Joule heating density, and maximal turbulent kinetic energy in the entire domain with different applied currents at 5000 s.

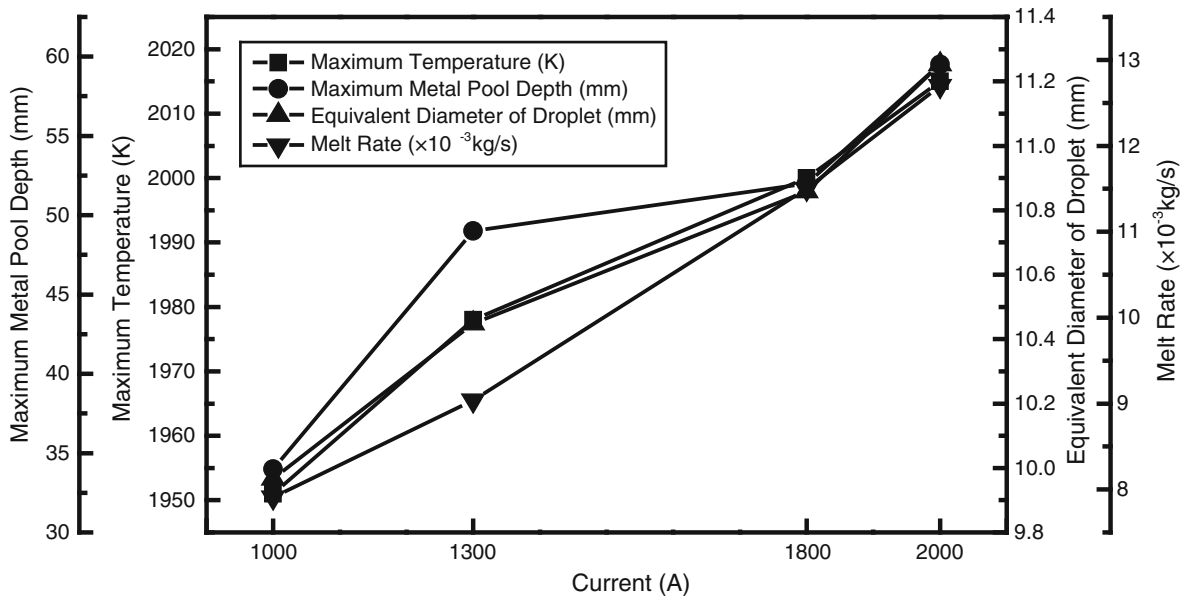


Fig. 13—Comparison of the maximum temperature, maximal metal pool depth, equivalent diameter of the metal droplet, and melt rate with different applied currents at 5000 s.

becomes more important, and the mean value also increases. The heat and momentum between the slag and metal pool are transferred fully when more current is applied. Figure 16 shows the varying of the turbulent kinetic energy and the temperature with time at point 2. The turbulent kinetic energy as well as the temperature in the metal pool also fluctuates due to the falling metal droplet. The turbulent kinetic energy and temperature increase with bigger applied current. It can be inferred that the metal in the pool becomes hotter and flows more intense with the increasing applied current.

We pay attention to the metal pool profiles as shown in Figure 11. The shapes of the metal pool

profiles are similar to that of the isotherms. A shallow U-shaped metal pool is formed with an 1000 A applied current. When the applied current increases to 1300 and 1800 A, the metal pool becomes the deep V-shaped due to more heat and momentum. With the applied current of 2000 A, the deep V-shaped metal pool is broadened to deep U-shaped metal pool. The maximal metal pool depth increases from 34.0 to 59.5 mm with the applied current ranging from 1000 to 2000 A. The defect such as macrosegregation and gas hole would appear with a deeper metal pool. Moreover, the deeper metal pool goes against the axial crystallization. Therefore, the applied current of

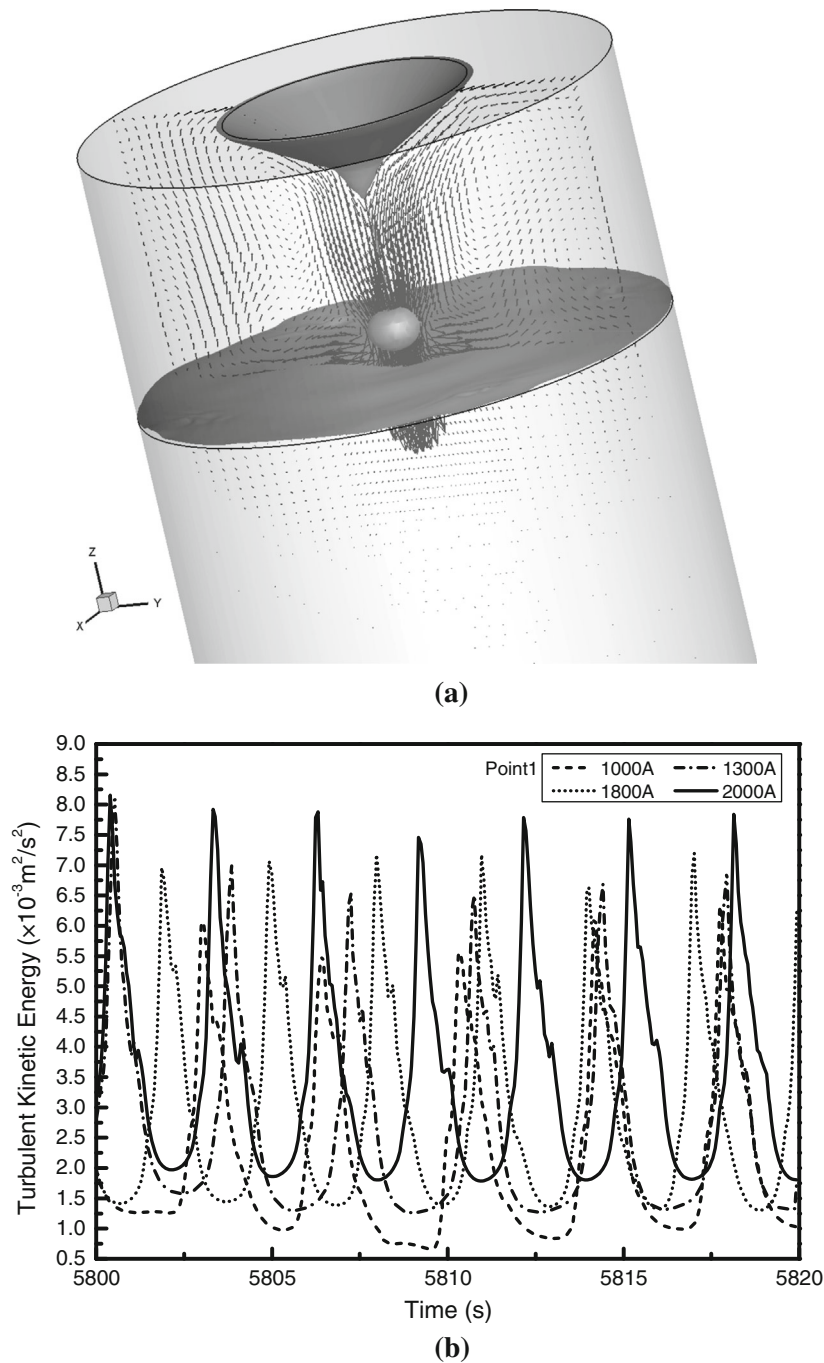


Fig. 14—(a) Falling metal droplet, slag/metal interface, and velocity field and (b) evolution of the turbulent kinetic energy with time at point 1 with different applied currents.

the ESR process should be designed carefully for a shallow U-shaped metal pool.

VI. CONCLUSIONS

A transient 3D finite-volume mathematical model has been developed to investigate the coupled electromagnetic, flow, temperature fields, and solidification in the ESR furnace considering the conducting in the mold.

The experiment is performed, and a reasonable agreement between the experimental observations and numerical results is obtained. The effect of applied current on the ESR process is clarified by the model. It is the first investigation of the coupled physical fields in the ESR process by a 3D model.

The principal findings are summarized as follows:

1. A part of the electric current in the slag passes through the mold, and this portion increases when more current is applied.

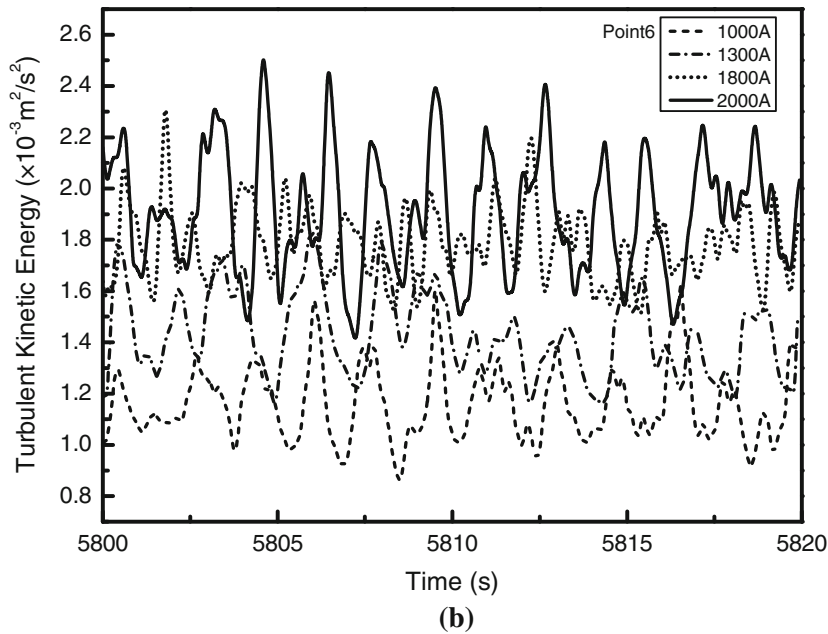
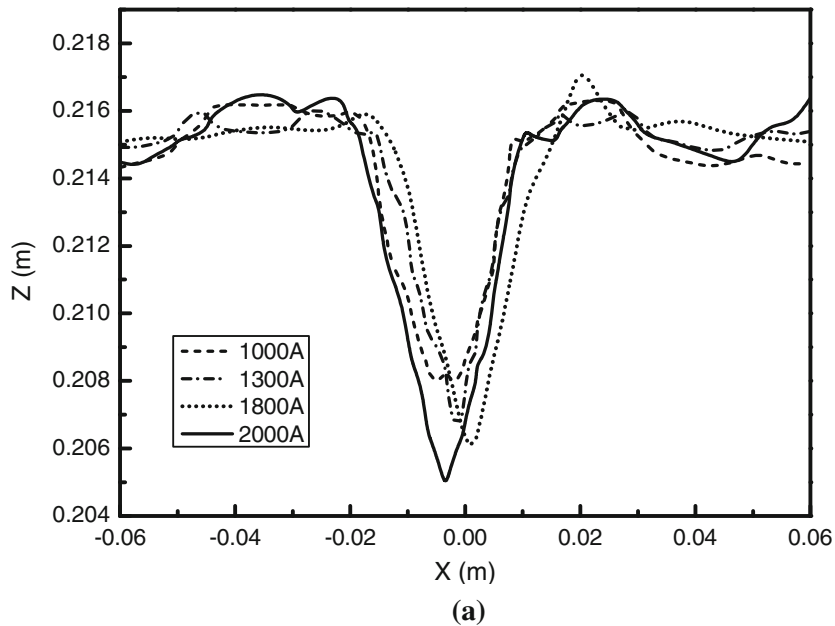
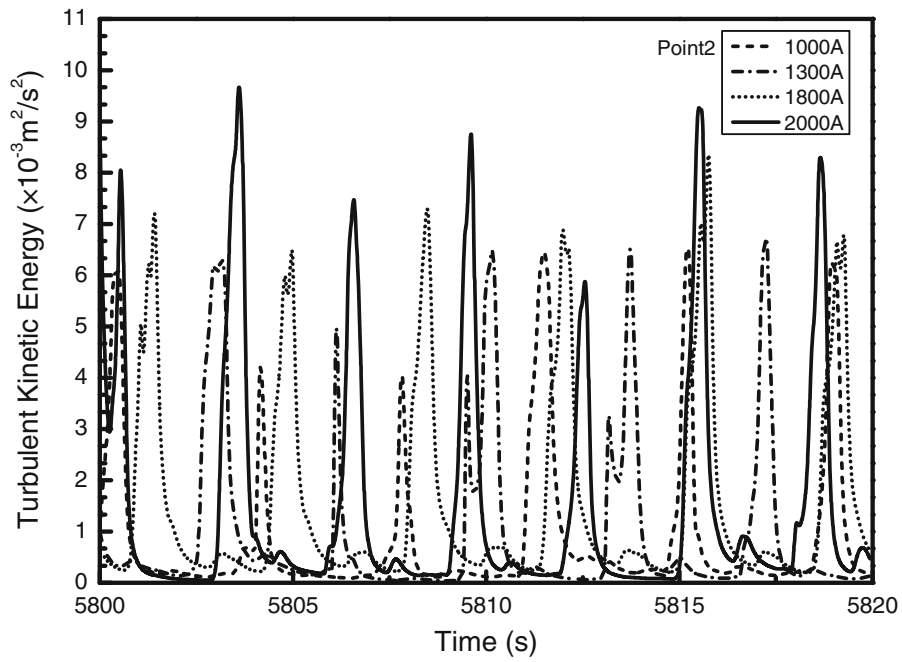


Fig. 15—(a) Deformation of the slag/metal interface with different applied currents and (b) varying of the turbulent kinetic energy with time at point 6 with different applied currents.

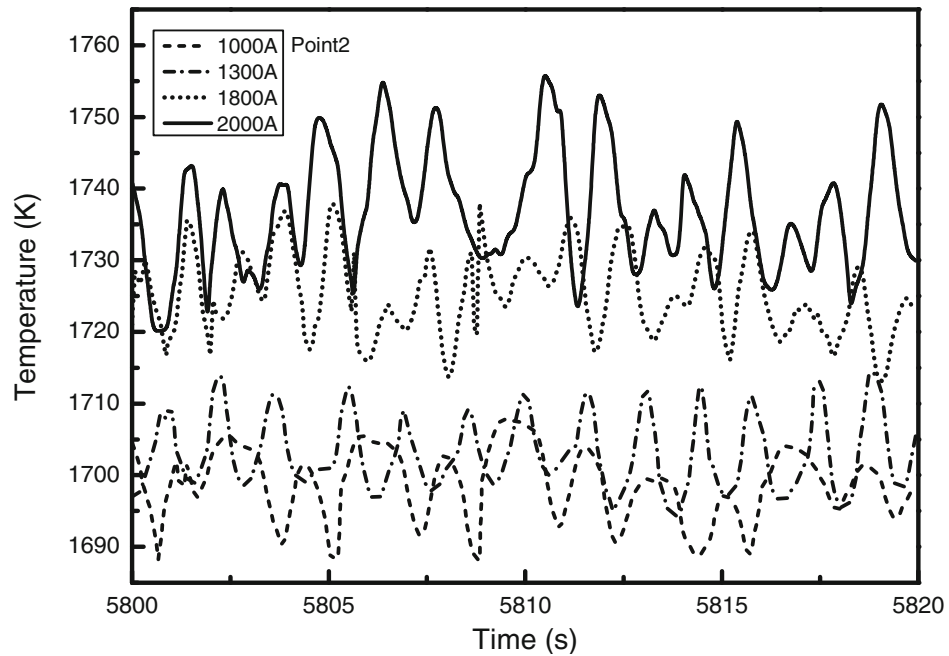
2. Joule heating and large EMF appear around the metal droplet, and the Joule effect and EMF change as they fall. The EMF tends to block the movement of the metal droplet.
3. The minimum Joule heating density is located in the outer side of the top and bottom of the slag. With the increasing current, the Joule heating density at the outer side of the top slag increases, while that at the bottom of the slag decreases.
4. The hotter region is found under the outer side of the electrode. The upper part of the slag at the outer side owns a higher temperature, while a lower heat generation is observed at the same location. The

isotherms in the metal are parabolic, and the curvature increases with a larger current.

5. The heat extracted by the cooling water results in a descending movement of the slag at the lateral wall due to buoyancy, driving a stable clockwise circulation. At the center of the slag, a counterclockwise circulation is caused by the EMF and falling metal droplets. The flow in the middle of the slag becomes stronger and slower closer to the lateral wall when more current is applied.
6. The shapes of the metal pool profiles are similar to that of the isotherms. The shallow U-shaped metal pool changes to the deep V-shaped metal pool with



(a)



(b)

Fig. 16—(a) Variation of the turbulent kinetic energy with time at point 2 with different applied currents and (b) variation of the temperature with time at point 2 with different applied currents.

the increasing current. The maximal metal pool depth increases from 34.0 to 59.5 mm with the current ranging from 1000 to 2000 A.

ACKNOWLEDGMENTS

The authors' gratitude goes to the National Natural Science Foundation of China [No. 51210007].

NOMENCLATURE

\vec{A}	Magnetic potential vector [(V s)/m]
A_{mush}	Mushy zone constant
\vec{B}	Magnetic flux density (T)
c_p	Heat capacity [J/(kg K)]
$C_{1\varepsilon}$	1.42
$C_{2\varepsilon}$	1.68
$C_{3\varepsilon}$	0.09
\vec{D}	Electric flux density (C/m ²)

\vec{E}	Electric field intensity (N/C)
f_H	Electric current frequency (Hz)
f_ℓ	Liquid fraction
\vec{F}_b	Buoyancy force (N/m ³)
\vec{F}_e	Electromagnetic force (N/m ³)
\vec{F}_{ed}	Effective electromagnetic force (N/m ³)
\vec{F}_p	Pressure drop (m/s)
\vec{g}	Gravitational acceleration (m ² /s)
G_k	Generation of turbulence kinetic energy due to the mean velocity gradients (Pa s)
G_b	Generation of turbulence kinetic energy due to buoyancy (Pa s)
h	Sensible enthalpy (J/kg)
\vec{H}	Magnetic field intensity (A/m)
H	Enthalpy (J/kg)
I_{rms}	Root mean square current (A)
J	Current density (A/m ²)
k	Turbulent kinetic energy (m ² /s ²)
k_{eff}	Effective thermal conductivity [W/(m K)]
L	Latent heat (J/kg)
p	Pressure (Pa)
Q_{Joule}	Joule heating (W)
R	Radius (m)
R_{max}	Radius of the mold (m)
R_e	Additional term of dissipation rate of turbulent kinetic energy (m ² /s ³)
S_k	Source term of solidification in the turbulent kinetic energy equation (m ² /s ³)
S_e	Source term of solidification in the dissipation rate of turbulent kinetic energy equation (m ² /s ³)
t	Time (s)
T	Temperature (K)
T_{ref}	Reference temperature (K)
T_s	Solidus temperature (K)
T_ℓ	Liquidus temperature (K)
\vec{u}	Velocity (m/s)
\vec{u}_{cast}	Casting velocity (m/s)
V_{drop}	Voltage drop of the lateral wall (V)
Y_M	Contribution of the fluctuating dilatation to the overall dissipation rate (m ² /s ³)

GREEK SYMBOLS

α	Volume fraction of fluid
α_k	Inverse effective Prandtl number for turbulent kinetic energy
α_e	Inverse effective Prandtl number for dissipation rate of turbulent kinetic energy
β	Thermal expansion coefficient (1/K)
δ	Electromagnetic skin thickness (m)
ε	Dissipation rate of turbulent kinetic energy (m ² /s ³)
η	Correction coefficient
μ	Magnetic permeability (F/m)
μ_{0m}	Vacuum permittivity of metal (F/m)
μ_{eff}	Effective viscosity (Pa s)
ρ	Density (kg/m ³)
ρ_{em}	Electric resistance of metal (Ω m)
σ	Electrical conductivity [1/(Ω m)]

σ_m	Electrical conductivity of the metal [1/(Ω m)]
σ_s	Electrical conductivity of the slag [1/(Ω m)]
ϕ	Electric potential (V)

REFERENCES

1. A.J.D. Johnson and A. Hellawell: *Metall. Trans.*, 1972, vol. 3, pp. 1016–19.
2. A. Mitchell and S. Joshi: *Metall. Trans.*, 1973, vol. 4, pp. 631–42.
3. M. Choudhary, J. Szekely, B.I. Medovar, and YU.G. Emelyanenko: *Metall. Trans. B*, 1982, vol. 13B, pp. 35–43.
4. A.H. Dilawari and J. Szekely: *Metall. Trans. B*, 1978, vol. 9B, pp. 77–87.
5. Y.M. Ferng, C.C. Chieng, and C. Pan: *Numer. Heat Transf. A*, 1989, vol. 16, pp. 429–49.
6. V. Weber, A. Jardy, B. Dussoubs, D. Ablitzer, S. Rybéron, V. Schmitt, S. Hans, and H. Poisson: *Metall. Mater. Trans. B*, 2009, vol. 42B, pp. 271–80.
7. B.K. Li, F. Wang, and F. Tsukihashi: *ISIJ Int.*, 2012, vol. 52 (7), pp. 1289–95.
8. A. Kharicha, A. Ludwig, and M. Wu: *Mater. Sci. Eng. A*, 2005, vol. 413, pp. 129–34.
9. B. Hernandez-Morales and A. Mitchell: *Ironmak. Steelmak.*, 1999, vol. 26 (6), pp. 423–38.
10. K. Miyazawa, T. Fukaya, S. Asai, I. Muchi, M. Choudhary, and J. Szekely: *Trans. ISIJ*, 1985, vol. 25, pp. 386–93.
11. K. Kajikawa, S. Ganesh, K. Kimura, H. Kudo, T. Nakamura, Y. Tanaka, R. Schwant, F. Gatazka, and Y. Ling: *Ironmak. Steelmak.*, 2007, vol. 34 (3), pp. 216–20.
12. M. Choudhary and J. Szekely: *Metall. Trans. B*, 1980, vol. 11B, pp. 439–53.
13. A.H. Dilawari, J. Szekely, and T.W. Eagar: *Metall. Trans. B*, 1978, vol. 9B, pp. 371–81.
14. A. Jardy, D. Ablitzer, and J.F. Wadier: *Metall. Trans. B*, 1991, vol. 22B, pp. 111–20.
15. M. Choudhary and J. Szekely: *Metall. Trans. B*, 1981, vol. 12B, pp. 418–21.
16. A.H. Dilawari and J. Szekely: *Metall. Trans. B*, 1977, vol. 8B, pp. 227–36.
17. O. Biro and K. Preis: *IEEE Trans. Magn.*, 1989, vol. 25 (4), pp. 3145–59.
18. K.M. Kelkar, S.V. Patankar, and A. Mitchell: *International Symposium on Liquid Metal Processing and Casting*, Santa Fe, 2005, pp. 137–44.
19. A. Kharicha, A. Mackenbrock, A. Ludwig, W. Schützenhöfer, V. Maronnier, M. Wu, and O. Köser: *International Symposium on Liquid Metal Processing and Casting*, Nancy, 2007, pp. 107–13.
20. A. Kharicha, W. Schützenhöfer, A. Ludwig, and G. Reiter: *Mater. Sci. Forum*, 2010, vol. 649, pp. 229–36.
21. C.W. Hirt and B.D. Nichols: *J. Comput. Phys.*, 1981, vol. 39 (1), pp. 201–25.
22. A. Rückert and H. Pfeifer: *International Scientific Colloquium Modelling for Electromagnetic Processing*, Hannover, 2008, pp. 27–9.
23. M. Meier, G. Yadigaroglu, and B.L. Smith: *Eur. J. Mech. B Fluids*, 2002, vol. 21, pp. 61–73.
24. A. Kharicha, W. Schützenhöfer, A. Ludwig, G. Reiter, and M. Wu: *Steel Res. Int.*, 2008, vol. 79 (8), pp. 632–36.
25. A. Kharicha, W. Schützenhöfer, A. Ludwig, G. Reiter, and M. Wu: *Int. J. Cast Met. Res.*, 2009, vol. 22, pp. 155–59.
26. A. Mitchell: *Mat. Sci. Eng. A*, 2005, vol. 413, pp. 10–18.
27. A. Mitchell: *Mater. Sci. Technol.*, 2009, vol. 25 (2), pp. 186–90.
28. C.R. Swaminathan and V.R. Voller: *Metall. Trans. B*, 1992, vol. 23B, pp. 651–64.
29. A. Kharicha, M. Wu, A. Ludwig, M. Ramprecht, and H. Holzgruber: *TMS: CFD Modeling and Simulation in Materials*, TMS, Orlando, 2012, pp. 139–46.
30. A.D. Patel: *International Symposium on Liquid Metal Processing and Casting*, Nancy, 2007, pp. 95–105.
31. A. Kharicha, A. Ludwig, and M. Wu: *International Symposium on Liquid Metal Processing and Casting*, Nancy, 2011, pp. 113–19.

32. S.A. Cefalu, K.J. Vanevery, and M.J.M. Krane: *TMS: Multiphase Phenomena and CFD Modeling and Simulation in Materials Processes*, TMS, Charlotte, 2004, pp. 279–83.
33. L. Nastac, S. Sundarraj, K. Yu, and Y. Pang: *JOM*, 1998, vol. 50 (3), pp. 30–35.
34. Y.Y. Sheng, G.A. Irons, and D.G. Tisdale: *Metall. Mater. Trans. B*, 1998, vol. 29B, pp. 85–94.
35. M. Hugo, B. Dussoubs, A. Jardy, J. Escaffre, and H. Poisson: *International Symposium on Liquid Metal Processing and Casting*, Austin, 2013, pp. 79–85.
36. M. Murgaš, A.S. Chaus, A. Pokusa, and M. Pokusová: *ISIJ Int.*, 2000, vol. 40 (10), pp. 980–6.
37. A. Mitchell and B. Hernandez-Morales: *Metall. Trans. B*, 1990, vol. 21B, pp. 723–31.